RSC Advances

PAPER

View Article Online
View Journal | View Issue

Check for updates

Cite this: *RSC Adv.*, 2025, **15**, 31651

Theoretical study on the mechanisms and kinetics of nitrous acid with the simplest aromatic Criegee intermediate

Guangliang Chen,[a] Mingqiang Huang,*[a] Guangzhen Gao,[b] Xingqiang Liu,[c] Changjin Hu,[d] Weixiong Zhao,[d] Xuejun Gu[d] and Weijun Zhang[d]

Received 16th May 2025
Accepted 6th August 2025

DOI: 10.1039/d5ra03441h

rsc.li/rsc-advances

Nitrous acid (HONO) is a vital pollutant gas and the nitrogen-containing organic compounds (NOCs) produced by its reaction are the main components of aerosols. The reaction mechanisms and kinetics of HONO and the simplest aromatic Criegee intermediate (PhCHOO) are investigated by density functional theory and transition state theory in this study. The results demonstrate that cycloaddition of HONO and PhCHOO to form heteroozonide with the highest activation energy and smallest rate constant does not easily occur. Pathways of oxygen atom transfer and cycloaddition can form *in situ* HNO_3 and benzoic acid. Meanwhile, the hydrogen atom transfer pathway results in the generation of phenyl hydroperoxide methyl nitrite (Ph-HPMN), which has the lowest activation energy, dominating the reaction between HONO and PhCHOO with a rate constant (5.68×10^{-13} cm^3 per molecule per s) close to that with OH radicals (4.83×10^{-12} cm^3 per molecule per s). These results provide a theoretical reference for clarifying the mechanism of generation of NOCs formed from ozonolysis of styrene and other olefin compounds in the presence of HONO.

1. Introduction

Nitrous acid (HONO), which originates from combustion processes, vehicle exhausts and biological sources, is an important trace gas in the tropospheric atmosphere.[1–3] In addition, HONO can be generated by the photolysis of nitrates or nitric acids.[4,5] Although the concentration of HONO is lower than that of other nitrogen oxides, it is comparable to the concentration of OH and other radicals present in the atmosphere.[6] The concentration of HONO typically varies between 0.1 and 10 ppb,[2,6–8] but in a contaminated atmosphere it can reach up to 20 ppb.[9] The photolysis of HONO produces OH and NO radicals. The formed OH radicals can promote the formation of pollutants such as ozone, peroxyacetyl nitrate and fine particulate matter ($PM_{2.5}$ particles), while NO radicals can participate in photooxidation reaction of volatile organic compounds to generate nitrogen-containing organic compounds (NOCs). Thus, HONO has an important impact on air quality.[10,11] It is worth mentioning that HONO can undergo bimolecular reactions with OH, Cl and ClO radicals.[6,12] Due to the lack of photolysis of HONO at night, its concentration becomes relatively high, and these bimolecular reactions become even more important at night.

Styrene, which is emitted into the atmosphere by human activities such as solvent use and automobile exhaust, is the second most highly reactive aromatic volatile organic compound (AVOC) in the field of environmental chemistry, second only to toluene.[13,14] Styrene itself is toxic and has potential mutagenic and carcinogenic properties. Exposure to styrene may cause damage to the central nervous system and reproductive system of the human body.[15] In addition, when emitted into the atmosphere, styrene mainly undergoes oxidation reactions with ozone. Ozone is first added to the vinyl C=C bond by 1,3-cycloaddition, generating a five-membered ring ozonation intermediate, which breaks C–C and O–O bonds to produce aldehydes, CH_2OO and other Criegee intermediates.[14,16,17] Researches have shown that except for isomerization and decomposition reactions, Criegee intermediates can stabilize through collision with other atmospheric species, and can undergo bimolecular reactions with trace gases such as H_2O, SO_2, NO, NO_2, HNO_3, *etc.*[18–21] The rate constant of bimolecular reaction for CH_2OO can be as high as 10^{-10} cm^3 per molecule per s. For example, for the reaction of $CH_2OO + HNO_3$, its rate constant is 5.1×10^{-10} cm^3 per molecule per s at 295 K.[21] The reaction between CH_2OO and HNO_3 produces excited intermediate nitrooxymethyl hydroperoxide ($NO_3CH_2OOH^*$), which

---

[a] *Fujian Provincial Key Laboratory of Modern Analytical Science and Separation Technology, College of Chemistry & Chemical Engineering and Environment, Minnan Normal University, Zhangzhou 363000, China. E-mail: huangmingqiang@mnnu.edu.cn*

[b] *College of Physics and Electronic Engineering, Jiangsu Normal University, Xuzhou 221116, China*

[c] *School of Environment Science & Engineering, Tan Kah Kee College, Xiamen University, Zhangzhou 363105, China*

[d] *Laboratory of Atmospheric Physico-Chemistry, Anhui Institute of Optics and Fine Mechanics, Chinese Academy of Sciences, Hefei 230031, China*

undergoes cleavage to generate OH radical and $CH_2(O)NO_3$ as a major reaction pathway, with a branch ratio as high as 0.79.[21]

$CH_2(O)NO_3$ and other NOCs are important components of secondary organic aerosol (SOA) particles.[22] These NOCs have strong stimulating effects and can cause brain and lung edema, induce DNA mutations, and pose a threat to health when absorbed by the human body.[22–24] Also, NOCs containing the N═O chromophore are a type of brown carbon with strong light absorption ability. They can absorb and scatter sunlight, resulting in reduced atmospheric visibility, and are one of the main culprits of haze pollution,[22,25] which has attracted widespread attention. Although various aromatic NOCs have been detected in field measurement experiments, the formation mechanism of NOCs still needs to be further studied. Styrene is the second most highly reactive AVOC, and SOA generated by its reaction with ozone is an important part of atmospheric anthropogenic SOA.[14,17] C_6H_5CHOO (PhCHOO) produced by styrene ozonation is the simplest aromatic Criegee intermediate. However, theoretical studies on the subsequent reaction of PhCHOO to produce NOCs have not been reported. Therefore, the generation process for PhCHOO produced by the ozonolysis of styrene is investigated in this study, and the formation mechanism of NOCs formed from the reaction of PhCHOO and HONO is further discussed in depth. These results provide a theoretical reference for the generation mechanism of NOCs produced by ozonolysis of styrene and other olefin compounds in the presence of HONO.

2. Computational methods

M06-2X is a commonly used density functional theory (DFT) calculation method, and its configuration obtained using CCSD(T) to calculate energy can provide more reliable results for common atmospheric chemical reactions.[20,26–28] The 6-311++G(d,p) basis set using DFT was found to be more efficient than the 6-31G(d) basis set.[29] Thus, Gaussian 09 software[30] was utilized to optimize the configurations of various species with M06-2X/6-311++G(d,p), and calculation of frequency and zero-point energy for each configuration were also carried out. The GaussView 5.0 feature in Gaussian 09 software[30] is used to obtain the optimized structure geometry visualization of each species. Furthermore, intrinsic reaction coordinate (IRC)[31] is performed to determine whether the resulting transition state is associated with corresponding reactants and products. Based on the optimized structure, CCSD(T)/6-311++G(3df,3pd)[32] is performed for calculation, and the higher precision energy of each configuration is obtained after correcting the zero-point energy. Cartesian coordinates and frequencies for all optimized structures at the M06-2X/6-311++G(d,p) level of theory are provided in Table S1 and Table S2 of the SI. The electronic energy (E) at M06-2X/6-311++G(d,p) and CCSD(T)/6-311++G(3df,3pd) level is listed in Table S3, and IRC profiles for the reactions at the M06-2X/6-311++G(d,p) level are illustrated in Fig. S1 of the SI.

The traditional transition state theory (TST) combined with zero curvature tunneling is exploited to calculate rate constant ($k(T)$) of each reaction path:[33,34]

$$k(T) = \kappa \frac{k_B T}{h} \frac{Q_{TS}}{Q_R} e^{-E_a/RT}$$

where κ is the zero curvature tunneling correction coefficient, E_a is reaction activation energy, and k_B, h and R represent Boltzmann's constant, Planck's constant and the ideal gas constant, respectively. Q_{TS} and Q_R are the partition function of transition state and reactant, respectively. κ and $k(T)$ for each path under certain temperature in kelvin are obtained using Polyrate 17.[35]

3. Results and discussion

3.1. Analysis of mechanism for ozonolysis of styrene

The reaction mechanism for ozonolysis of styrene is investigated firstly. The configurations of transition state and product optimized using M06-2X/6-311++G(d,p) and potential energy surface (PES) obtained at CCSD(T)/6-311++G(3df,3pd) are shown in Fig. 1. An ozone molecule is close and added to vinyl C═C bond in styrene, generating a five-membered ring ozonation intermediate of C1 *via* transition state TS1. The distances between the C atom in the C═C bond of styrene and the O atom in ozone in TS1 are 2.339 Å and 2.209 Å, respectively, showing a tendency to form a five-membered ring adduct. The imaginary frequency of TS1 is 288i cm^{-1}, corresponding to the vibration of ozone's O atom attacking the C atom of C═C bond. The IRC calculation results show that TS1 is associated with the corresponding reactants (styrene and ozone) and product (C1) (see Fig. S1(a) in SI). For the single-point energy calculations of various species at the CCSD(T)/6-311++G(3df,3pd) level, the obtained T1 diagnostic values are listed in Table S3 of the SI, none of which exceed 0.02 (boundary value of closed-shell systems).[36] In addition, the T1 diagnostic value of each transition state is less than 0.02, indicating that multireference characters for the transition state can be ignored.[27,36] The activation energy and reaction energy of each reaction calculated at the CCSD(T) level are offered in Table S4 of the SI. Compared to the reactants styrene and ozone, the energy barrier of TS1 is 1.46 kcal mol^{-1}, and reaction energy is −68.43 kcal mol^{-1} (see Table S4), which are close to the results reported in experimental studies.[16] Due to its low energy barrier and high reaction heat, the ozonolysis of styrene is more likely to occur under atmospheric conditions.

The generated C1 intermediate produces formaldehyde, benzaldehyde and Criegee intermediates (C_6H_5CHOO (PhCHOO) and CH_2OO) by breaking the bonds of C–C and O–O through TS2A and TS2B subsequently. As illustrated in Fig. S1(b) and (c) in the SI, TS2A and TS2B are connected with corresponding reactants and products. The distance between two C atoms of vinyl in these two transition states is 1.882 Å and 1.900 Å, respectively, while the lengths of O⋯O are 1.976 Å and 1.981 Å, presenting the breaking trend of C–C and O–O bond (see Fig. 1). The imaginary frequencies of TS2A and TS2B are 546i and 557i cm^{-1}, respectively, which correspond to breaking vibrations of C–C and O–O bonds. Compared to C1 intermediate, the energy barrier for producing formaldehyde and PhCHOO is 18.79 kcal mol^{-1}, with reaction energy of −2.17 kcal mol^{-1}. The energy barrier and reaction energy for

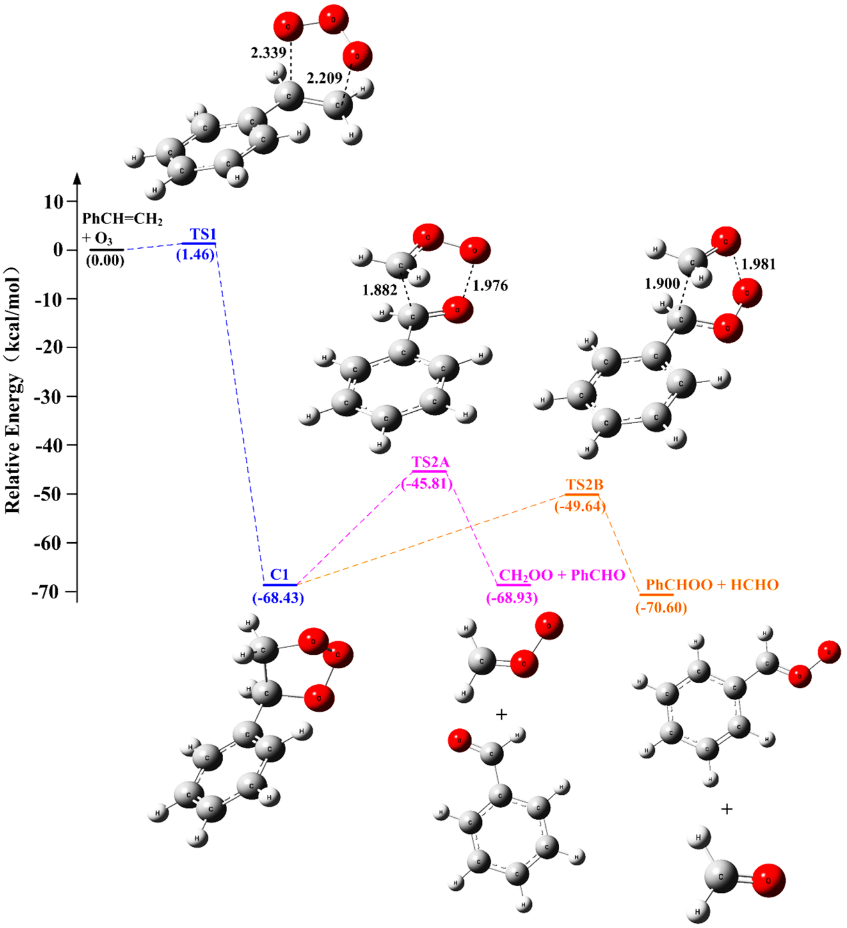

Fig. 1 Optimized configurations at M06-2X/6-311++G(d,p) level and potential energy surface at CCSD(T)/6-311++G(3df,3pd) level for ozonolysis of styrene (bond lengths: Å).

generation of benzaldehyde and CH_2OO are 22.62 and -0.50 kcal mol^{-1}, respectively (see Fig. 1 and Table S4). Due to the low energy barrier and high reaction heat for producing formaldehyde and PhCHOO, it is the main reaction channel for ozonolysis of styrene. Therefore, the mechanism of the reaction of PhCHOO and HONO is investigated in the following sections.

HONO exists in two forms: *trans*- and *cis*-HONO. Calculated results in this work show that at the theoretical level for CCSD(T)/6-311++G(3df,3pd)//M06-2X/6-311++G(d,p), *trans*-HONO is 0.48 kcal mol^{-1} more stable than *cis*-HONO, which is relatively consistent with the research results reported by Guo *et al.*,[37] indicating that the calculation method adopted in this work can provide accurate and reliable energy values. PhCHOO formed by the cleavage of C1 intermediate also has two forms: *cis*- and *trans*-PhCHOO. According to the theoretical calculation research results of Anglada *et al.*[38] and Taatjes *et al.*,[39] compared

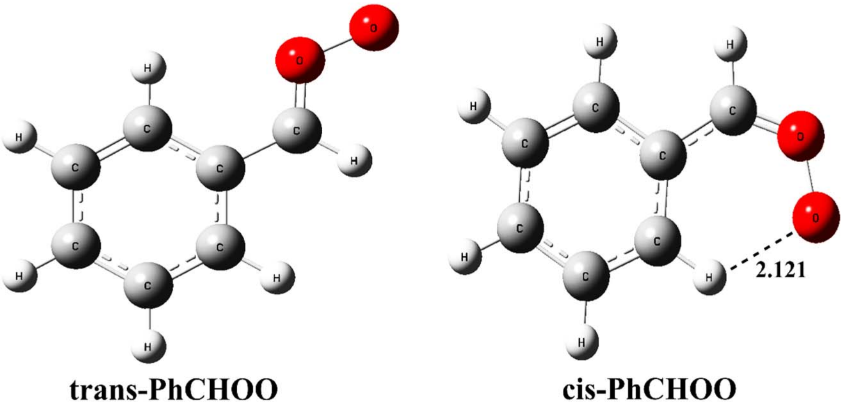

Fig. 2 Optimized configurations at M06-2X/6-311++G(d,p) level for *trans*-PhCHOO and *cis*-PhCHOO (bond length: Å).

with *syn*-CH_3CHOO, *anti*-CH_3CHOO has a smaller steric hindrance and is more likely to form corresponding adducts with H_2O, SO_2, *etc.* The configurations of *anti*-PhCHOO and *syn*-PhCHOO optimized at the M06-2X/6-311++G(d,p) level are shown in Fig. 2. This is similar to the result of Du *et al.*,[40] where *anti*-PhCHOO is 0.55 kcal mol^{-1} more stable than *syn*-PhCHOO at the level of CCSD(T)/6-311++G(3df,3pd)//M06-2X/6-311++G(d,p). It can be seen from Fig. 2 that the terminal O atom of *syn*-PhCHOO is close to the benzene ring, and the distance between it and a hydrogen atom in the benzene ring is 2.121 Å, forming an O⋯C–H hydrogen bond. Thus, *syn*-PhCHOO has a large steric hindrance and is not conducive to the reaction with HONO. On the contrary, the terminal O atom of *anti*-PhCHOO is far away from the benzene ring and has a smaller steric hindrance, making it easier to react with HONO. For the reactions of *syn*-PhCHOO with *anti*-HONO or *cis*-HONO, Gaussian 09 software[30] is used to search for and optimize adducts and transition states with M06-2X/6-311++G(d,p) multiple times, but it failed to afford the corresponding adducts and transition states. Therefore, the *trans*-PhCHOO conformation is selected as the initial reactant to study the mechanism of its reaction with *cis*- and *trans*-HONO.

3.2. Reaction mechanism for formation of HNO_3

Trans-PhCHOO can undergo oxygen atom transfer reaction with *cis*-HONO and *trans*-HONO. In this reaction pathway, the terminal O atom of *trans*-PhCHOO is shifted to the N atom of HONO to form HNO_3 and benzaldehyde through transition states *trans*-TSot and *cis*-TSot, as displayed in Fig. 3. Compared to *trans*-PhCHOO, O–O bond lengths in the two transition states are extended by 0.364 Å and 0.347 Å, respectively. The lengths for O–N are 1.894 Å and 1.855 Å, respectively, showing a trend of generating benzaldehyde and HNO_3. The imaginary frequencies of *trans*-TSot and *cis*-TSot are 598i and 660i cm^{-1}, respectively, which correspond to stretching vibrations for O–O and O–N. The IRC calculation results show that *trans*-TSot and *cis*-TSot are associated with corresponding reactants and products (see Fig. S1(d) and (e) in SI). As illustrated in Fig. 4 and 5, the reaction energy of oxygen atom transfer reactions for *trans*-PhCHOO and HONO is −69.83 kcal mol^{-1}, and the activation energy for *trans*-PhCHOO + *trans*-HONO reaction relative to the reactants is 8.25 kcal mol^{-1} (see Fig. 4). The activation energy for *trans*-PhCHOO + *cis*-HONO is up to 16.98 kcal mol^{-1} (see Fig. 5).

The rate constant corrected by the zero curvature tunneling effect for each reaction pathway calculated using Polyrate 17 [35] in the temperature range of 238–338 K is listed in Table 1. The rate constant (k_{ot}) of the oxygen atom transfer path for *trans*-PhCHOO and *trans*-HONO changes from 4.67×10^{-23} to 1.82×10^{-20} cm^3 per molecule per s. While the k_{ot} value corresponding to *trans*-PhCHOO and *cis*-HONO varies from 2.48×10^{-28} to 6.62×10^{-24} cm^3 per molecule per s in the range 238–338 K. Especially at 298 K, k_{ot} for the *trans*-PhCHOO + *trans*-HONO reaction (2.57×10^{-21} cm^3 per molecule per s) is higher than that for the *trans*-PhCHOO + *cis*-HONO reaction (2.40×10^{-25} cm^3 per molecule per s), about 4 orders of magnitude higher.

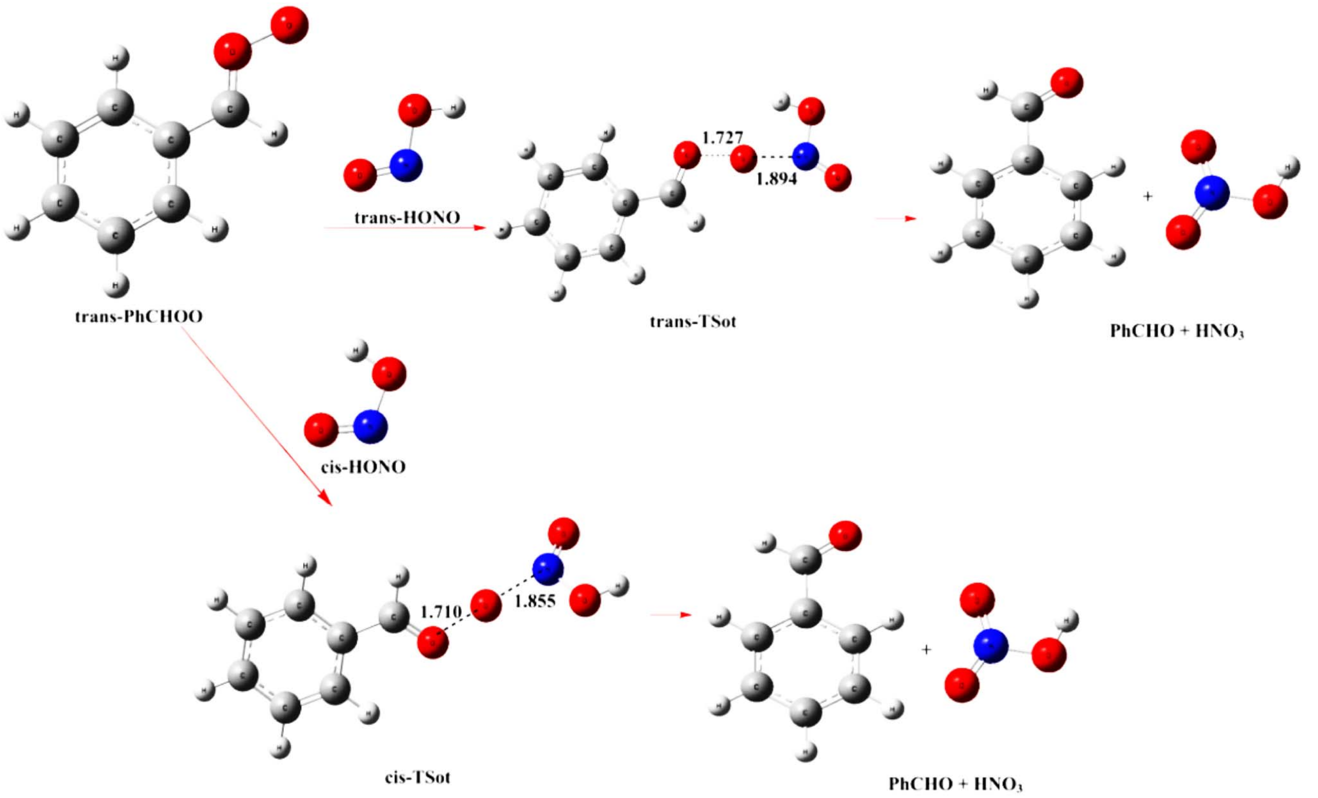

Fig. 3 Optimized configurations at M06-2X/6-311++G(d,p) level for oxygen atom transfer reaction of *trans*-PhCHOO and HONO (bond lengths: Å).

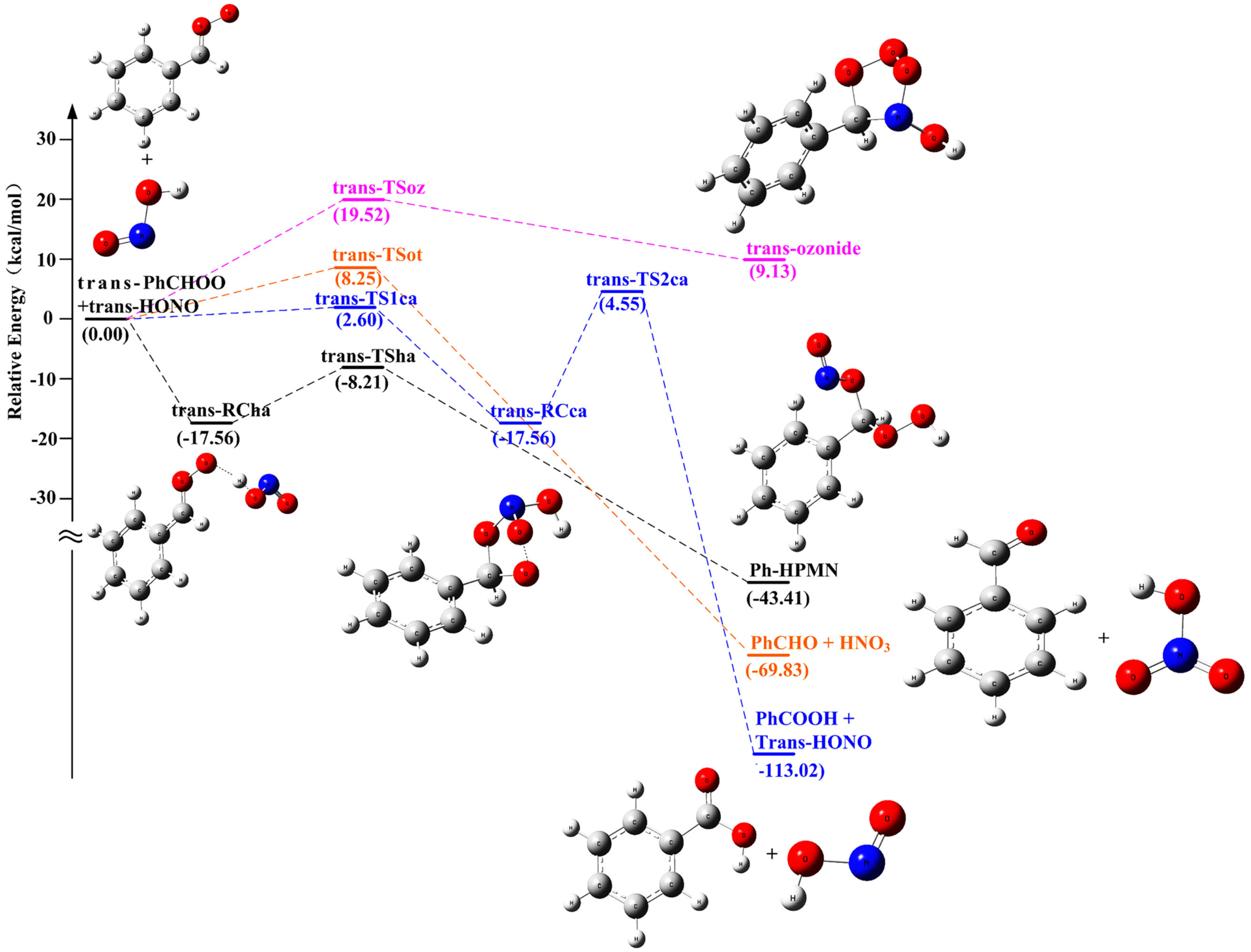

Fig. 4 Potential energy surface at CCSD(T)/6-311++G(3df,3pd) level for the reaction of *trans*-PhCHOO and *trans*-HONO.

The Arrhenius diagram for each reaction channel at 238–338 K is described in Fig. 6 and 7, respectively. Based on Arrhenius diagrams, the activation energy (E_a) of the oxygen atom transfer path for *trans*-PhCHOO and *trans*-HONO is calculated to be 4.90 kcal mol^{-1}, which is lower than the E_a for *trans*-PhCHOO + *cis*-HONO reaction (8.28 kcal mol^{-1}). This indicates that the oxygen atom transfer path for *trans*-PhCHOO and *trans*-HONO is the main channel for producing benzaldehyde and HNO$_3$.

3.3. Reaction mechanism for formation of benzoic acid

Two kinds of cycloaddition reactions can occur between *trans*-PhCHOO and HONO. Mechanistically, in both reactions, it is the cycloaddition of 1,3-dipole of carbon and terminal oxygen of CHOO in *trans*-PhCHOO to NO bond of HONO that produces the dipole–dipole complex and leads to the generation of a five-membered ring adduct (see Fig. 8–10). Vereecken *et al.*[41] have studied the cycloaddition reaction between Criegee intermediate and NO, RO$_2$, and SO$_2$, and also reported the formation of a five-membered cycloadduct, which was referred to as heteroozonide.

The transition states of *trans*-TSoz and *cis*-TSoz for heteroozonides generated by terminal O and C atoms of *trans*-PhCHOO combine with O and N atoms of HONO in the first type of cycloaddition reaction, as displayed in Fig. 8. The IRC profiles displayed in Fig. S1(f) and (g) of the SI clearly demonstrate that *trans*-TSoz and *cis*-TSoz connect the corresponding reactants and products. The distance of the terminal O atom of PhCHOO and O atom of HONO in the two transition states is 1.917 Å and 1.894 Å, while the distance between the C atom in CHOO and N atom of HONO is 1.746 Å and 1.651 Å, showing the trend towards the formation of a five-membered ring adduct. The imaginary frequencies of *trans*-TSoz and *cis*-TSoz are 366i and 248i cm^{-1}, respectively, which correspond to vibrations of terminal O and C atoms in *trans*-PhCHOO attacking O and N atoms of HONO. As displayed in Fig. 4 and 5, the energy barrier for heteroozonide generated by the reaction of *trans*-PhCHOO with *trans*-HONO and *cis*-HONO is 19.52 and 15.31 kcal mol^{-1}, respectively. It is worth noting that these two reactions are endothermic, with reaction energies of 9.13 and 10.16 kcal mol^{-1}, which do not easily occur under atmospheric conditions.

In the second type of cycloaddition reaction, two steps lead to the formation of benzoic acid. In the first step, a five-membered ring adduct (RCca) is formed between *trans*-

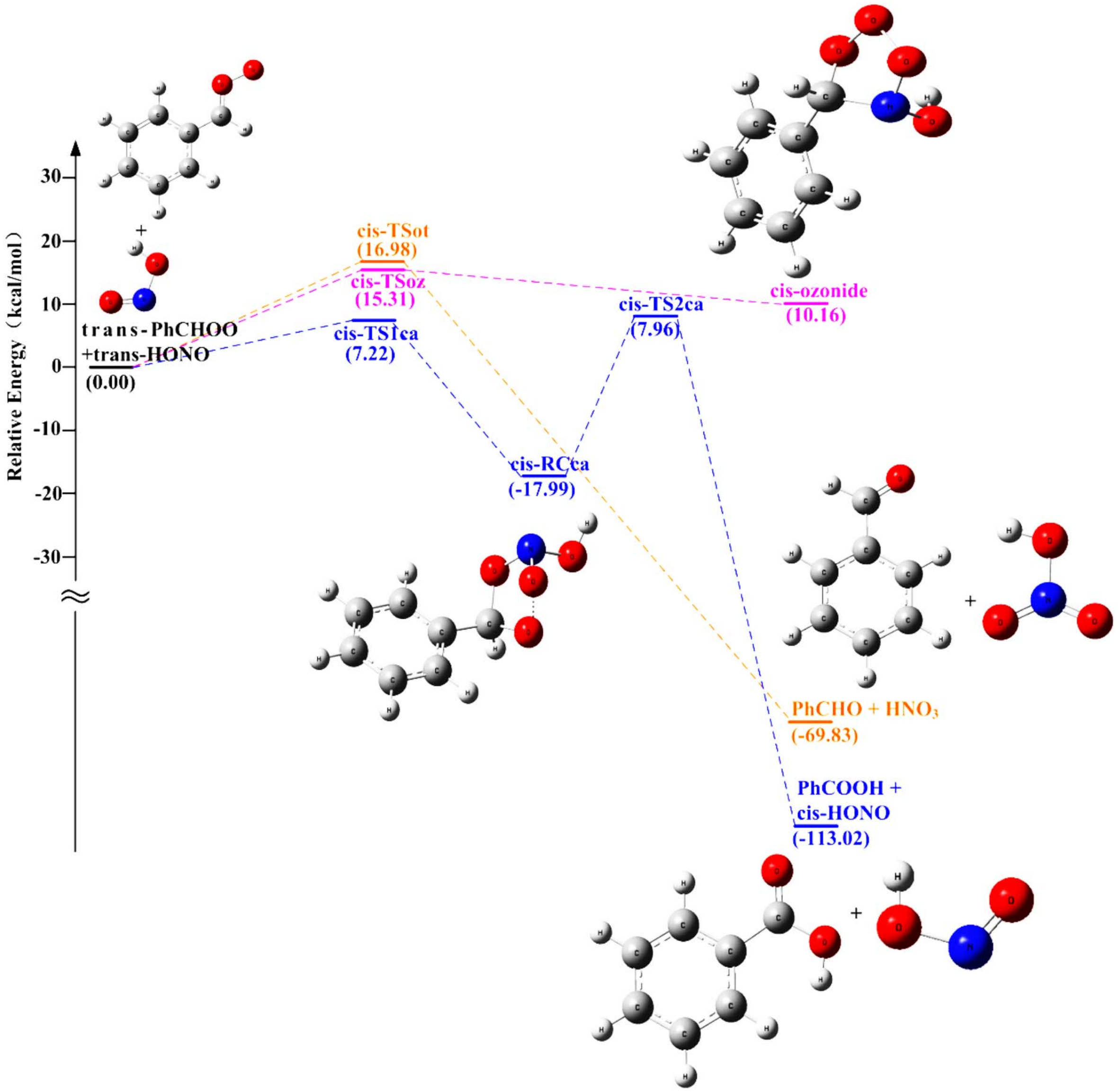

Fig. 5 Potential energy surface at CCSD(T)/6-311++G(3df,3pd) level for the reaction of *trans*-PhCHOO and *cis*-HONO.

Table 1 Rate constant corrected by the tunneling effect for each reaction pathway at 238–338 K (cm^3 per molecule per s)

	Trans-PhCHOO + *trans*-HONO				*Trans*-PhCHOO + *cis*-HONO		
T (K)	k_{ot}	k_{oz}	k_{ca}	k_{ha}	k_{ot}	k_{oz}	k_{ca}
238	4.67×10^{-23}	5.58×10^{-35}	4.69×10^{-25}	6.85×10^{-12}	2.48×10^{-28}	3.82×10^{-32}	5.62×10^{-29}
248	1.03×10^{-22}	3.41×10^{-34}	7.08×10^{-25}	5.19×10^{-12}	9.65×10^{-28}	1.95×10^{-31}	1.24×10^{-28}
258	2.14×10^{-22}	1.82×10^{-33}	1.04×10^{-24}	3.02×10^{-12}	3.41×10^{-27}	8.76×10^{-31}	2.57×10^{-28}
268	4.23×10^{-22}	8.57×10^{-33}	1.48×10^{-24}	1.66×10^{-12}	1.10×10^{-26}	3.53×10^{-30}	5.08×10^{-28}
278	8.02×10^{-22}	3.62×10^{-32}	2.07×10^{-24}	9.47×10^{-13}	3.29×10^{-26}	1.29×10^{-29}	9.54×10^{-28}
288	1.46×10^{-21}	1.39×10^{-31}	2.82×10^{-24}	7.15×10^{-13}	9.18×10^{-26}	4.33×10^{-29}	1.72×10^{-27}
298	2.57×10^{-21}	4.88×10^{-31}	3.78×10^{-24}	5.68×10^{-13}	2.40×10^{-25}	1.34×10^{-28}	2.99×10^{-27}
308	4.37×10^{-21}	1.58×10^{-30}	4.98×10^{-24}	3.52×10^{-13}	5.93×10^{-25}	3.86×10^{-28}	5.03×10^{-27}
318	7.21×10^{-21}	4.77×10^{-30}	6.45×10^{-24}	2.26×10^{-13}	1.39×10^{-24}	1.04×10^{-27}	8.19×10^{-27}
328	1.16×10^{-20}	1.35×10^{-29}	8.24×10^{-24}	1.02×10^{-13}	3.10×10^{-24}	2.65×10^{-27}	1.29×10^{-26}
338	1.82×10^{-20}	3.59×10^{-29}	1.03×10^{-23}	8.93×10^{-14}	6.62×10^{-24}	6.39×10^{-27}	2.01×10^{-26}

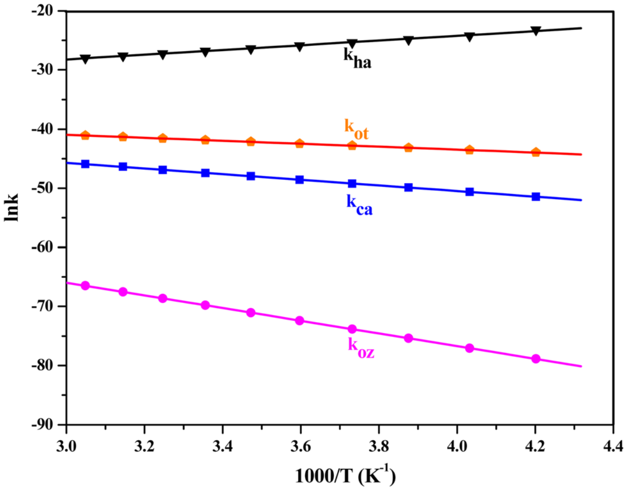

Fig. 6 Arrhenius diagram of each channel for the reaction of *trans*-PhCHOO and *trans*-HONO at 238–338 K.

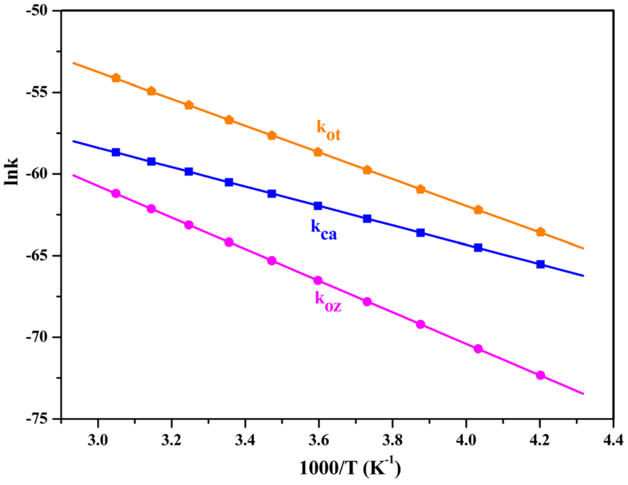

Fig. 7 Arrhenius diagram of each channel for the reaction of *trans*-PhCHOO and *cis*-HONO at 238–338 K.

PhCHOO and HONO *via* transition state of *trans*-TS1ca or *cis*-TS1ca. Compared with *trans*-TSoz and *cis*-TSoz shown in Fig. 8, in the above two transition states, the terminal O and C atoms of *trans*-PhCHOO combine with N and O atoms of HONO to form RCca. The distance of the terminal O atom of PhCHOO and N atom of HONO in the two transition states is 1.945 Å and 1.915 Å, while the distance between the C atom of CHOO and O atom of HONO is 1.879 Å and 1.924 Å (see Fig. 9 and 10), showing the trend towards the formation of a five-membered ring adduct. The imaginary frequencies of *trans*-TS1ca and *cis*-TS1ca are 363i and 368i cm^{-1}, respectively, which correspond to vibrations of terminal O and C atoms in *trans*-PhCHOO attacking N and O atoms of HONO. IRC curves of *trans*-TS1ca and *cis*-TS1ca show that they are associated with corresponding reactants and products (see Fig. S1(h) and (i) in SI). Relative to the reactants *trans*-PhCHOO and *trans*-HONO, the energy barrier for formation of RCca is 2.60 kcal mol^{-1}, with reaction energy of −17.56 kcal mol^{-1}, while the energy barrier for *trans*-PhCHOO and *cis*-HONO to produce RCca is 7.22 kcal mol^{-1}, with reaction energy of −17.99 kcal mol^{-1} (see Fig. 4 and 5).

In the subsequent second reaction step, the five membered ring adduct RCca is converted to benzoic acid and HONO through transition state *trans*-TS2ca or *cis*-TS2ca. The imaginary frequencies of *trans*-TS2ca and *cis*-TS2ca are 1099i and 1206i cm^{-1}, respectively, which correspond to stretching vibrations for N–O and O–H bonds. As illustrated in Fig. 9 and 10, in these two transition states, the O⋯N distance is 1.682 Å and 1.590 Å, C⋯H distance is 1.206 Å and 1.209 Å, and O⋯H distance is 1.543 Å and 1.524 Å, respectively, showing the trend of N–O and C–H breaking and forming benzoic acid and HONO. *Trans*-TS2ca and *cis*-TS2ca are confirmed to be connected with corresponding reactants and products by IRC curves as displayed in Fig. S1(j) and (k) of the SI. Compared to *trans*-PhCHOO and HONO, the energy barrier for generation of benzoic acid is 4.55 kcal mol^{-1} (for *trans*-TS2ca) and 7.96 kcal mol^{-1} (for *cis*-TS2ca), with reaction energy of −113.02 kcal mol^{-1} (see Fig. 4 and 5).

It should be noted that with RCca as the initial stationary point, the energy barrier for generation of benzoic acid is 22.11 kcal mol^{-1} (for *trans*-TS2ca) and 25.95 kcal mol^{-1} (for *cis*-TS2ca), with reaction energy of −95.46 kcal mol^{-1} (for *trans*-RCca) and −95.03 kcal mol^{-1} (for *cis*-RCca) (see Fig. 4 and 5). The second step actually has a higher energy barrier, which is the rate-controlled step for cycloaddition reaction leading to benzoic acid formation. Rate constants for generation pathways of heteroozonide (k_{oz}) and benzoic acid (k_{ca}) in the temperature range of 238–338 K using Polyrate 17 [35] are shown in Table 1. The k_{oz} of heteroozonide produced by reaction of *trans*-PhCHOO and *trans*-HONO ranges from 5.58×10^{-35} to 3.59×10^{-29} cm^3 per molecule per s, while k_{oz} values of *trans*-PhCHOO and *cis*-HONO to generate heteroozonide change from 3.82×10^{-32} to 6.39×10^{-27} cm^3 per molecule per s in the range 238–338 K. k_{oz} for reaction of *trans*-PhCHOO and *cis*-HONO is about 3 orders of magnitude higher than that corresponding to *trans*-HONO.

On the contrary, k_{ca} for benzoic acid produced by reaction of *trans*-PhCHOO and *trans*-HONO ranges from 4.69×10^{-25} to 1.03×10^{-23} cm^3 per molecule per s, which is about 4 orders higher than the corresponding k_{ca} of *cis*-HONO (5.62×10^{-29} to 2.01×10^{-26} cm^3 per molecule per s) in the range 238–338 K. It is worth noting that when RCca is taken as the initial stationary point of the reaction, the energy barrier for generation benzoic acid is higher than that for formation of heteroozonide, but its reaction energy is −95.46 kcal mol^{-1} (for *trans*-RCca) or −95.03 kcal mol^{-1} (for *cis*-RCca), which is an exothermic reaction (while the production of heteroozonide is an endothermic reaction). Thus, the rate constant of the reaction of *trans*-PhCHOO with HONO to produce benzoic acid is always higher than rate constant of the heteroozonide formation path. According to the Arrhenius diagrams in Fig. 6 and 7, E_a of *trans*-PhCHOO and HONO to produce heteroozonide is 10.92 kcal mol^{-1} (for *trans*-HONO) and 9.87 kcal mol^{-1} (for *cis*-HONO). While, compared to *trans*-PhCHOO and HONO, E_a for benzoic acid formation pathway is 4.63 kcal mol^{-1} (for *trans*-HONO) and 7.35 kcal mol^{-1} (for *cis*-HONO). It should be

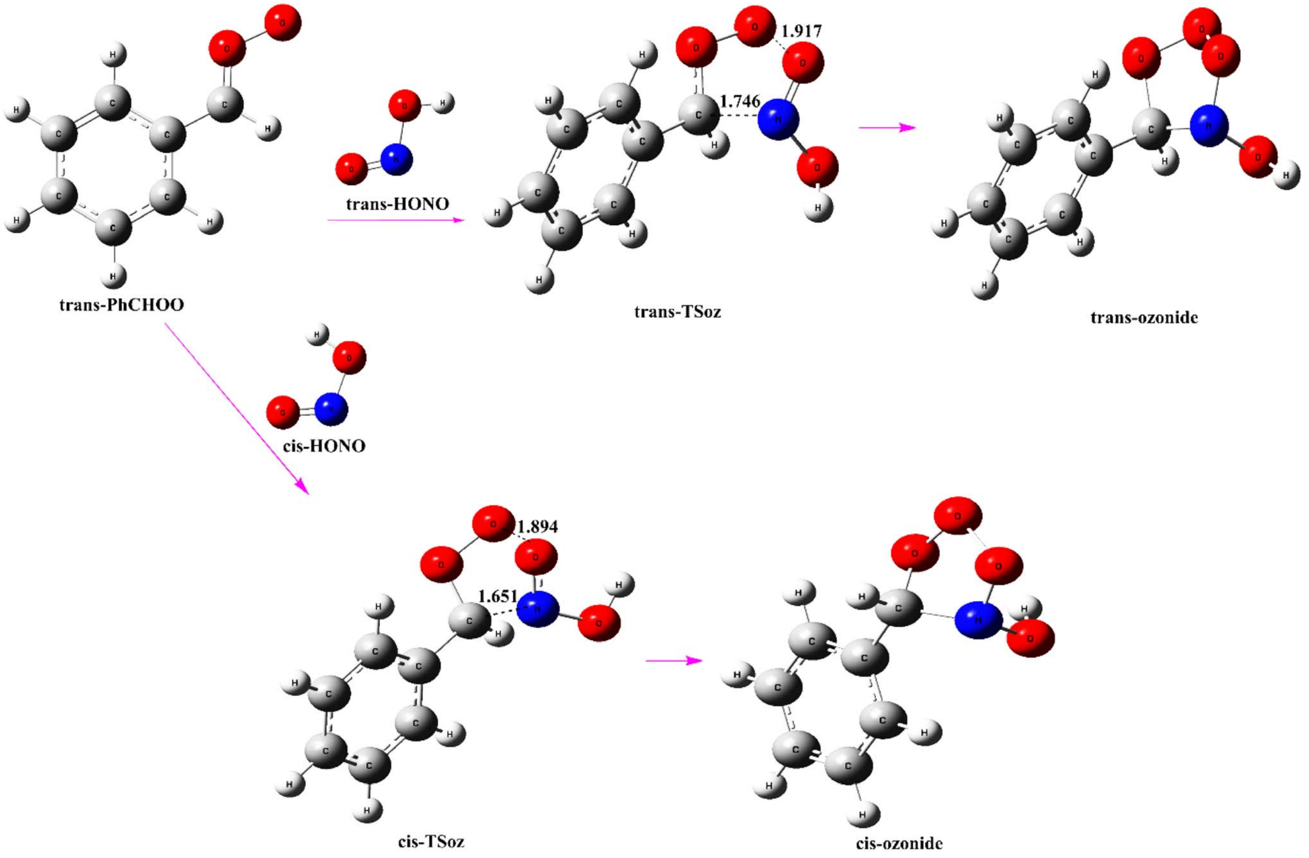

Fig. 8 Optimized configurations at M06-2X/6-311++G(d,p) level for the first type of cycloaddition reaction of *trans*-PhCHOO and HONO (bond lengths: Å).

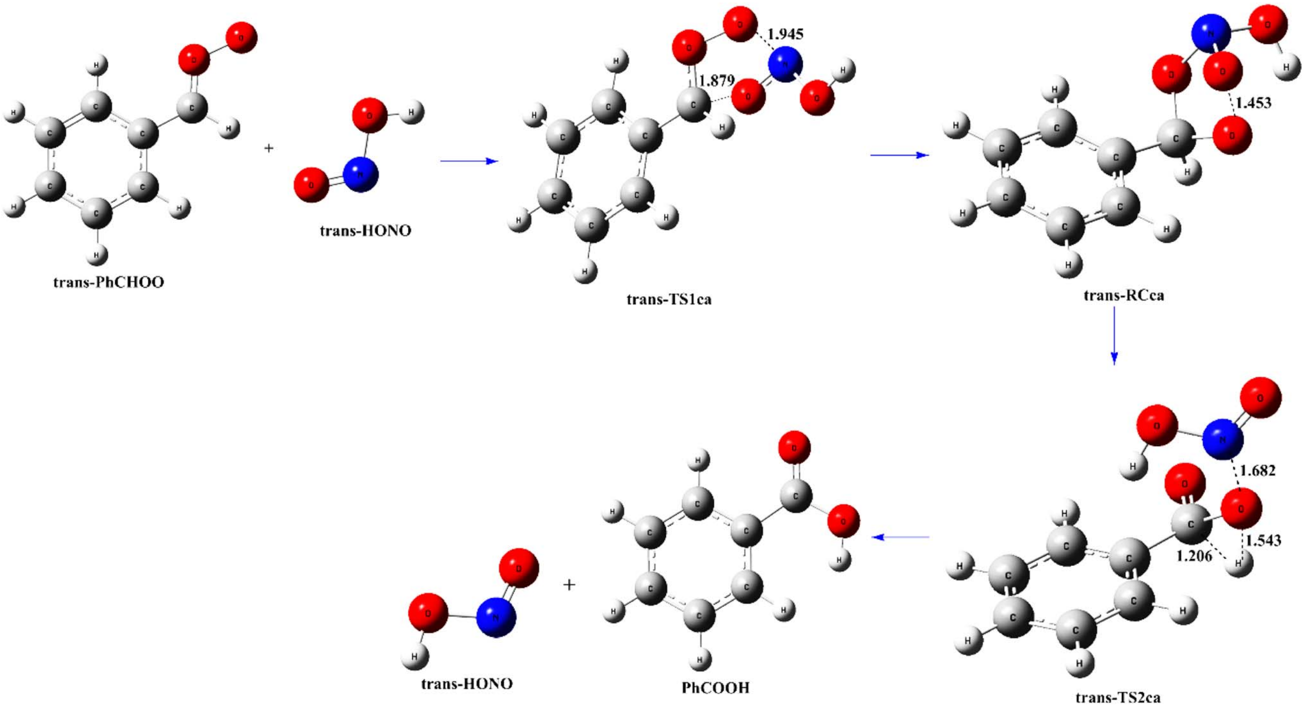

Fig. 9 Optimized configurations at M06-2X/6-311++G(d,p) level for the second type of cycloaddition reaction of *trans*-PhCHOO and *trans*-HONO (bond lengths: Å).

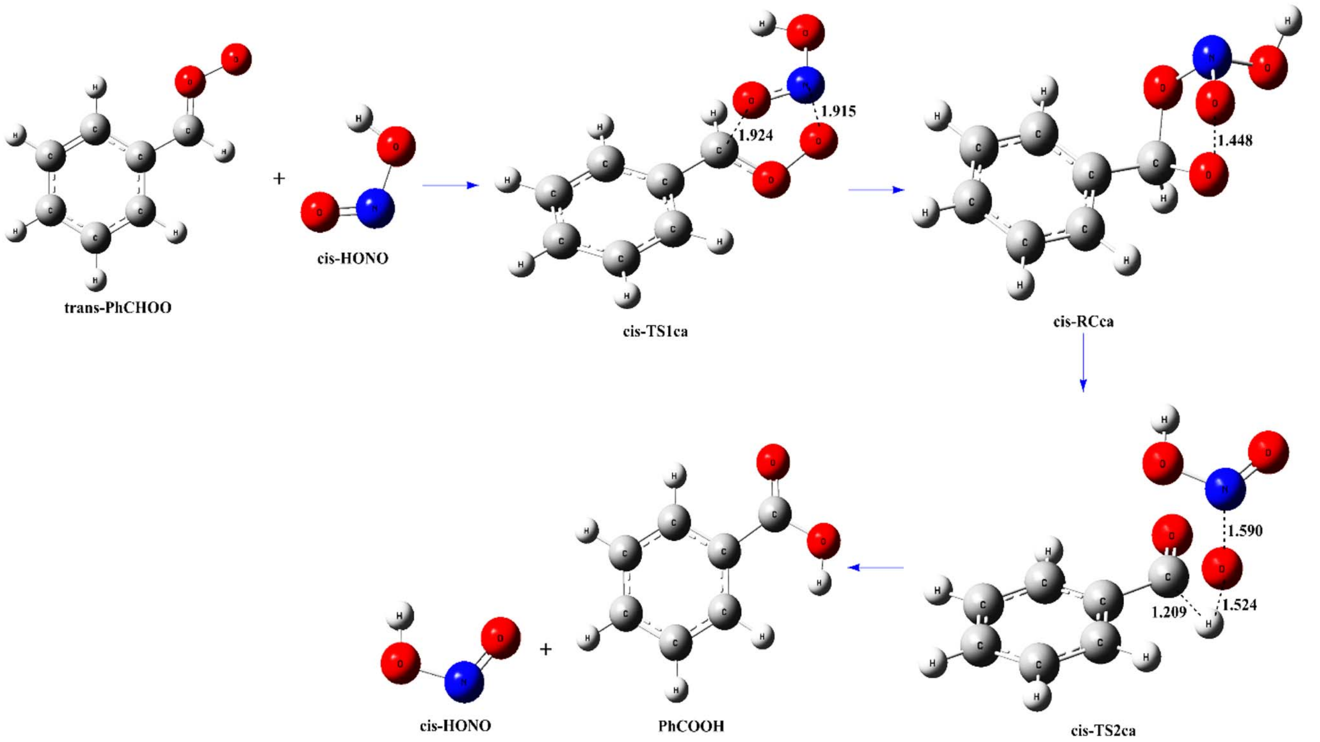

Fig. 10 Optimized configurations at M06-2X/6-311++G(d,p) level for the second type of cycloaddition reaction of *trans*-PhCHOO and *cis*-HONO (bond lengths: Å).

pointed out that for the reaction of *trans*-PhCHOO and HONO to produce heteroozonide with higher E_a, its k_{oz} is smaller than that of the benzoic acid formation path. This reaction pathway is almost impossible to occur under atmospheric conditions. The cycloaddition reaction between *trans*-PhCHOO and HONO mainly generates benzoic acid.

3.4. Reaction mechanism for formation of NOCs

Hydrogen atom transfer (HAT) reaction also can occur between *trans*-PhCHOO and HONO. The H atom of HONO transfers to the O atom at the end of *trans*-PhCHOO, while the C atom of the CHOO group in *trans*-PhCHOO attacks the O atom of HONO to form C–O, producing a final product of phenyl hydroperoxide methyl nitrite (Ph-HPMN) (see Fig. 11). The HAT pathway can also be seen as addition of O–H in HONO to the CHOO group of *trans*-PhCHOO, which is very similar to the 1,3-dipole addition of CH_2OO to HNO_3 proposed by Raghunath *et al.*[21] As shown in Fig. 11, *trans*-HONO is close to *trans*-PhCHOO and forms a pre-reaction complex of *trans*-RCha. In this complex, the distance of O···H in HONO is 1.018 Å, and the distance between the O atom at the end of PhCHOO and the H atom of HONO is 1.556 Å. The stable energy for forming *trans*-RCha is -17.56 kcal mol^{-1} (see Fig. 4), which undergoes a single-molecule transformation to produce Ph-HPMN *via trans*-TSha. The IRC curve illustrated in Fig. S1(l) of the SI indicates that it is connected with corresponding reactants and products. The distance between O atom and H atom of HONO in *trans*-TSha is extended to 1.361 Å, and the distance between the terminal O atom of PhCHOO and H atom of HONO is shortened to 1.105 Å. The distance between the C atom of the CHOO group in *trans*-PhCHOO and the O atom of the nitro group of HONO is 2.330 Å, showing the tendency of hydrogen transfer and C–O bond formation to produce Ph-HPMN (see Fig. 11). The imaginary frequency of *trans*-TSha is 218i cm^{-1}, which corresponds to stretching vibrations for O–H and C–O bonds. With respect to *trans*-PhCHOO and *trans*-HONO, the energy barrier of the HAT reaction is -8.21 kcal mol^{-1}, which is much lower than that of other reaction channels for *trans*-PhCHOO + HONO reactions (see Fig. 4).

It should be pointed out that it may be more accurate to consider the stable complex of *trans*-RCha as the initial stationary point for oxygen atom transfer, cycloaddition, and HAT reaction profiles, since dissociation of the complex must occur for these reactions to proceed. However, regrettably, for oxygen transfer and cycloaddition reactions, taking *trans*-RCha as the initial stationary point of the reaction, Gaussian 09 software[30] is utilized to search and optimize repeatedly, but it failed to afford the corresponding transition states. Furthermore, regarding the reactions of *anti*-PhCHOO and *cis*-HONO, multiple searches and optimizations are also conducted, but do not lead to the complex *cis*-RCha. Taking *anti*-PhCHOO and *anti*-HONO (or *cis*-HONO) as the initial stationary point of the reaction, transition states of *trans*-TSot, *cis*-TSot, *trans*-TSoz, *cis*-Tsoz, *trans*-TS1ca and *cis*-TS1ca are obtained. The IRC curves shown in Fig. S1(d)–(i) of the SI indicate that these transition states connect the corresponding reactants and products. Therefore, *anti*-PhCHOO and *anti*-HONO (or *cis*-HONO) are

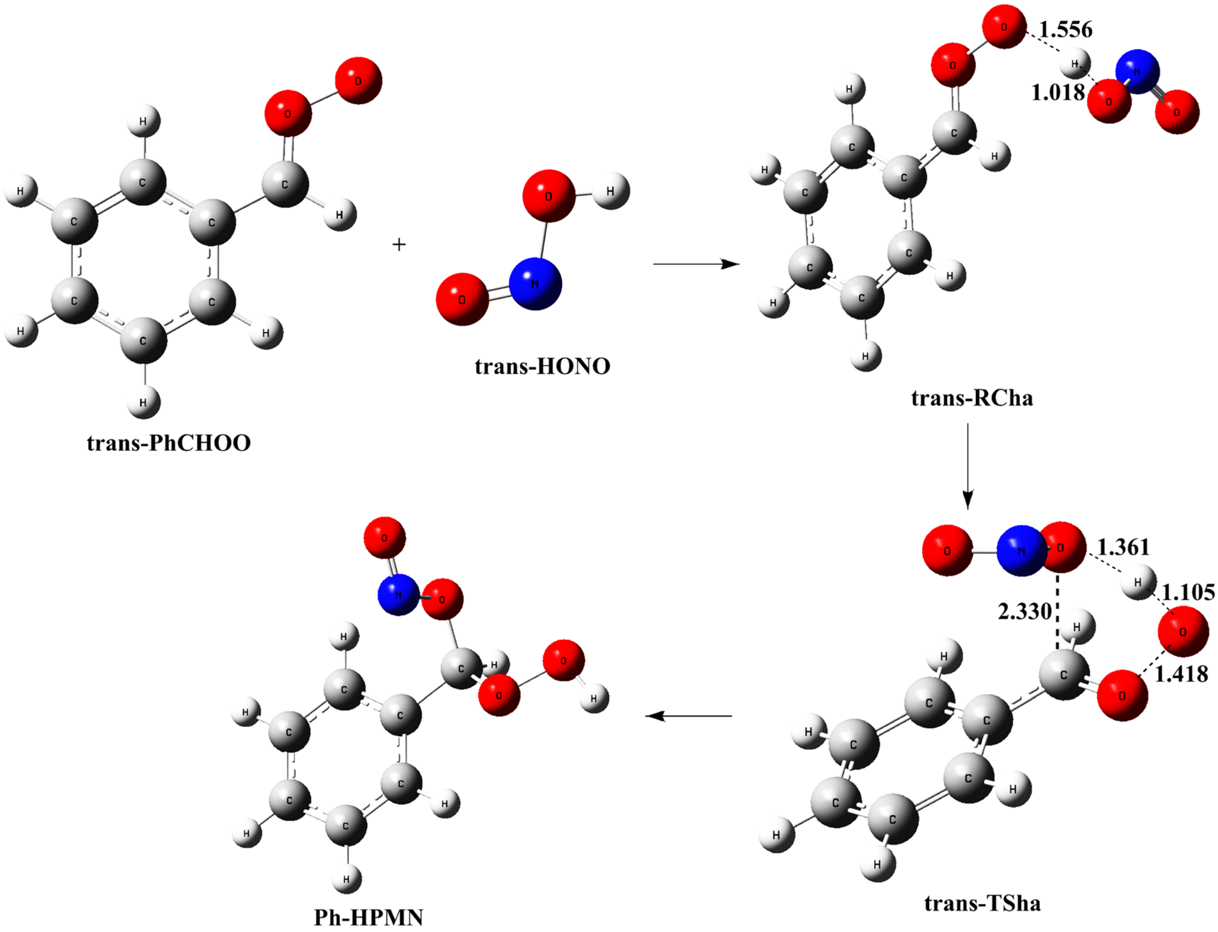

Fig. 11 Optimized configurations at M06-2X/6-311++G(d,p) level for hydrogen atom transfer reaction of *trans*-PhCHOO and *trans*-HONO (bond lengths: Å).

used as the initial stationary point to better compare and analyze the pathways of oxygen transfer, cycloaddition and HAT reactions.

It should be pointed out that with *trans*-RCha as the initial stationary point for HAT, the reaction energy barrier is 9.35 kcal mol^{-1} (see Fig. 4). *Trans*-HONO is close to *trans*-PhCHOO and forms pre-reaction complex *trans*-RCha, whose equilibrium constant is K_{eq}. *Trans*-RCha then generates Ph-HPMN through *trans*-TSha, with rate constant of k_2:

$$\textit{Trans}\text{-PhCHOO} + \textit{trans}\text{-HONO} \overset{K_{eq}}{\rightleftarrows} \textit{trans}\text{-RCha} \xrightarrow{k_2} \text{Ph-HPMN}$$

The rate constant of hydrogen transfer reaction (k_{ha}) is equal to the product of K_{eq} and k_2 ($k_{ha} = K_{eq} \times k_2$).[33,34] K_{eq} and rate constants (k_2 and k_{ha}) corrected by the zero curvature tunneling effect for the hydrogen transfer reaction pathway calculated using Polyrate 17 [35] in the range 238–338 K are provided in Table S5 of the SI. Values of k_{ha} are also listed in Table 1. In the temperature range of 238–338 K, k_{ha} changes from 8.93×10^{-14} to 6.85×10^{-12} cm^3 per molecule per s. Especially at 298 K, k_{ha} for the HAT reaction is 5.68×10^{-13} cm^3 per molecule per s, which is about 8 orders of magnitude higher than k_{ot} of the oxygen atom transfer reaction (2.57×10^{-21} cm^3 per molecule per s), and is about 11 orders of magnitude higher than k_{ca} for the benzoic acid formation pathway (3.78×10^{-24} cm^3 per molecule per s). In addition, the Arrhenius diagram as shown in Fig. 6 indicates that the HAT path dominates compared to other reaction paths in the range 238–338 K. As displayed in Fig. 6, the difference between rate constants of k_{ha} and those of other paths decreases as temperature increases. This is mainly because the activation energy of the HAT reaction is negative ($E_a = -2.49$ kcal mol^{-1}, compared to *trans*-PhCHOO and *trans*-HONO), exhibiting anti-Arrhenius behavior, while the activation energy of other reaction paths is positive, presenting Arrhenius behavior. It is worth noting that multiple optimizations in *trans*-PhCHOO and *cis*-HONO reaction did not afford the corresponding complex and transition state of Ph-HPMN in this work. The HAT reaction is only feasible in the case of *trans*-HONO, but does not occur for *cis*-HONO (see Fig. 4 and 11). Both the computational result in this work and experimental value reported in the literature[37] show that *trans*-HONO is more stable than *cis*-HONO, and HONO mainly exists in the form of *trans*-HONO. Compared with other reaction paths, the HAT reaction between *trans*-PhCHOO and *trans*-HONO has a higher rate constant, which dominates the reaction between HONO and PhCHOO.

It is well known that Cl, OH and ClO radicals are the main oxidants in the troposphere and can undergo oxidation reactions with HONO.[6] Since the rate constant of the HAT reaction is about 8–18 orders of magnitude higher than that of other pathways, for evaluating the relative influence of PhCHOO on HONO, only the HAT reaction path is selected for comparison with HONO reactions with Cl, OH and ClO radicals. The rate constant of the reaction of PhCHOO with HONO at 298 K (5.68×10^{-13} cm^3 per molecule per s) is about 4 orders of magnitude higher than that of the reaction of ClO radical with HONO (1.62×10^{-17} cm^3 per molecule per s) obtained by Anglada *et al.*[6] and about 2 orders of magnitude lower than that of the reaction of Cl radical with HONO (7.38×10^{-11} cm^3 per molecule per s). It is worth noting that rate constant of the reaction between PhCHOO and HONO obtained in this work is slightly smaller than that between OH radical and HONO (4.83×10^{-12} cm^3 per molecule per s).[6] This indicates that the reaction between PhCHOO and HONO can occur under atmospheric conditions, which can compete with reaction between HONO and OH radicals.

However, it should be pointed out that in evening or early morning, the concentration of OH is low,[42] and the reaction between PhCHOO and HONO may be an important chemical reaction process for the consumption of HONO at night, affecting the budget of atmospheric HONO. In addition, Ph-HPMN formed by the reaction of PhCHOO and HONO is a common nitrogen-containing organic component with strong light absorption ability in atmospheric aerosol particles. It can be clearly seen from Fig. 11 that Ph-HPMN contains a peroxy bond, which can be dissociated in the atmosphere to generate OH radicals and serve as the reservoir for OH radicals at night.[43] The results of this work indicate that the HAT pathway forms Ph-HPMN with the minimum activation energy and the maximum reaction rate constant, which dominates the reaction between HONO and PhCHOO. These results provide a theoretical basis for clarifying the formation mechanism of NOCs produced by ozonolysis of styrene and other olefin compounds in the presence of HONO.

4. Conclusions

The reaction mechanisms of HONO and the simplest aromatic Criegee intermediate PhCHOO were studied by the quantum chemistry method in this study. The results show that under atmospheric conditions, the HAT path produces the NOC Ph-HPMN, which has the smallest activation energy, and its reaction rate constant is about 8–18 orders of magnitude higher than that of other pathways. The reaction path of oxygen atom transfer and cycloaddition to form a five-membered cycloadduct generates nitric acid and benzoic acid as the final products, but the rate constants of these two channels are relatively small and do not play an important role in the atmosphere. Ph-HPMN is mainly generated by the reaction between HONO and PhCHOO. Its formation rate constant (5.68×10^{-13} cm^3 per molecule per s) is close to that of the reaction between OH radicals and HONO (4.83×10^{-12} cm^3 per molecule per s) at 298 K. Under atmospheric conditions, the reaction of PhCHOO with HONO can compete with the reaction of HONO and OH radicals. These results provide a reference and inspiration for the study of NOCs produced by the oxidation reaction of HONO.

Author contributions

Conceptualization: G. L. Chen and M. Q. Huang. Resources: C. J. Hu, W. X. Zhao and X. J. Gu. Writing – review and editing: G. L. Chen, M. Q. Huang, G. Z. Gao and X. Q. Liu. Supervision: W. J. Zhang. Funding acquisition: G. Z. Gao and M. Q. Huang. All the authors have read and agreed to the published version of the manuscript.

Conflicts of interest

We declare that we do not have any commercial or associative interest that represents a conflict of interest in connection with the work.

Data availability

The data supporting this article, such as activation energy and reaction energy of each reaction, Cartesian coordinates and frequencies for all optimized structures, have been included as part of the SI.

Supplementary information is available. Cartesian coordinates and frequencies for all optimized structures at M06-2X level are provided in Table S1 and S2. Electronic energy at M06-2X and CCSD(T) level, T1 diagnostic value for various species at CCSD(T) level are listed in Table S3. While, activation energy and reaction energy of each reaction at CCSD(T)level are offered in Table S4. Keq, rate constant (k2 and kha) corrected by tunneling effect for hydrogen atom transfer reaction path in 238–338 K are supplied in Table S5. Also, IRC profile for the reactions at M06-2X level are illustrated in Fig. S1. See DOI: **https://doi.org/10.1039/d5ra03441h**.

Acknowledgements

This work is supported by the National Natural Science Foundation of China (no. 42275136) and the Natural Science Foundation of Fujian Province of China (no. 2025J01972, 2021J01987). The authors express our gratitude to the referees for their valuable comments.

References

1 L. L. Li, Y. Z. Li, Y. N. Hu, J. W. Zhang, W. Du, S. Gligorovski and J. P. Liu, *Build. Environ.*, 2025, **269**, 112476.
2 D. Y. Chen, L. Zhou, S. Liu, C. F. Lian, W. G. Wang, H. F. Liu, C. Y. Li, Y. L. Liu, L. Luo, K. Xiao, Y. Chen, Y. Qiu, Q. W. Tan, M. F. Ge and F. M. Yang, *Sci. Total Environ.*, 2023, **903**, 166605.

3 R. Oswald, T. Behrendt, M. Ermel, D. Wu, H. Su, Y. Cheng, C. Breuninger, A. Moravek, E. Mougin, C. Delon, B. Loubet, A. Pommerening-Röser, M. Sörgel, U. Pöschl, T. Hoffmann, M. O. Andreae, F. X. Meixner and I. Trebs, *Science*, 2013, **341**, 1233–1235.

4 S. T. Andersen, L. J. Carpenter, C. Reed, J. D. Lee, R. Chance, T. Sherwen, A. Vaughan, J. Stewart, P. Edwards, W. Bloss, R. Sommariva, L. R. Crilley, L. Neves, K. Read, D. E. Heard, P. W. Seakins, L. K. Whalley, G. A. Boustead, L. T. Fleming, D. Stone and K. W. Fomba, *Sci. Adv.*, 2023, **9**, eadd6266.

5 M. Gen, Z. C. Liang, R. F. Zhang, B. R. Go and C. K. Chan, *Environ. Sci.: Atmos.*, 2022, **2**, 111–127.

6 J. M. Anglada and A. Sole, *J. Phys. Chem. A*, 2017, **121**, 9698–9707.

7 K. Toriyama, K. Fukae, Y. Suda, T. Kiyose, T. Oda, Y. Fujii, N. D. T. Chi, D. H. Huy, T. T. Hien and N. Takenaka, *Atmos. Environ.*, 2019, **214**, 116895.

8 X. Li, C. Ye, K. D. Lu, C. Y. Xue, X. Li and Y. H. Zhang, *Environ. Sci. Technol.*, 2024, **58**, 13035–13046.

9 Y. F. Jiang, M. Xia, L. K. Xue, X. F. Wang, X. L. Zhong, Y. C. Liu, M. Kulmala, T. Ma, J. Q. Wang, Y. R. Wang, J. Gao and T. Wang, *Environ. Sci. Technol.*, 2024, **58**, 14361–14371.

10 G. Sarwar, C. Hogrefe, B. H. Henderson, R. Mathur, R. Gilliam, A. B. Callaghan, J. Lee and L. J. Carpenter, *Sci. Total Environ.*, 2024, **917**, 170406.

11 H. Y. Ran, J. W. Zhang, Y. Qu, J. Yang, Y. Chen, Y. Sun, C. Y. Xue, Y. J. Mu and J. L. An, *Atmos. Environ.*, 2025, **348**, 121114.

12 S. S. Tang and L. Du, *Environ. Sci. Pollut. Res.*, 2019, **26**, 27842–27853.

13 V. K. Pal, S. Lee, M. Naidu, C. Lee and K. Kannan, *Environ. Int.*, 2022, **167**, 107449.

14 S. S. Yu, L. Jia, Y. F. Xu and Y. P. Pan, *Chemosphere*, 2024, **349**, 140811.

15 Z. Pilevar, A. Bahrami, S. Beikzadeh, H. Hosseini and S. M. Jafari, *Trends Food Sci. Technol.*, 2019, **91**, 248–261.

16 D. Johnsona and G. Marston, *Chem. Soc. Rev.*, 2008, **37**, 699–716.

17 L. Chiappini, E. Perraudin, N. Maurin, B. Picquet-Varrault, W. Y. Zheng, N. Marchand, B. Temime-Roussel, A. Monod, A. Le Person, F. Bernard, G. Eyglunent, A. Mellouki and J. F. Doussin, *J. Phys. Chem. A*, 2019, **123**, 1469–1484.

18 M. A. H. Khan, C. J. Percival, R. L. Caravan, C. A. Taatjes and D. E. Shallcross, *Environ. Sci.: Processes Impacts*, 2018, **20**, 437–453.

19 D. Stone, M. Blitz, L. Daubney, N. U. Howes and P. Seakins, *Phys. Chem. Chem. Phys.*, 2014, **16**, 1139–1149.

20 B. Long, J. L. Bao and D. G. Truhlar, *J. Am. Chem. Soc.*, 2016, **138**, 14409–14422.

21 P. Raghunath, Y. P. Lee and M. Lin, *J. Phys. Chem. A*, 2017, **121**, 3871–3878.

22 K. S. Jang, M. Choi, M. H. Park, M. H. Park, Y. H. Kim, J. J. Seo, Y. J. Wang, M. Hu, M. S. Bae and K. H. Park, *Environ. Pollut.*, 2020, **265**, 114870.

23 C. Wei, Y. M. Han, B. A. M. Bandowe, J. J. Cao, R. J. Huang, H. Y. Ni, J. Tian and W. Wilcke, *Sci. Total Environ.*, 2015, **505**, 814–822.

24 W. L. Fan, T. Chen, Z. L. Zhu, H. Zhang, Y. L. Qiu and D. Q. Yin, *J. Hazard. Mater.*, 2022, **430**, 128406.

25 A. Laskin, J. Laskin and S. A. Nizkorodov, *Chem. Rev.*, 2015, **115**, 4335–4382.

26 J. Elm, M. Bilde and K. V. Mikkelsen, *J. Chem. Theory Comput.*, 2012, **8**, 2071–2077.

27 X. F. Tan, L. Zhang and B. Long, *Phys. Chem. Chem. Phys.*, 2020, **22**, 8800–8807.

28 X. Lin, M. Q. Huang, M. C. Zhu, W. X. Zhao and W. J. Zhang, *Comput. Theor. Chem.*, 2023, **1219**, 113950.

29 Z. M. Kotena, M. Razi and S. Ahmadi, *J. Mol. Model.*, 2021, **27**, 315.

30 M. J. Frisch, G. W. Trucks, H. B. Schlegel, G. E. Scuseria, M. A. Robb, J. R. Cheeseman, G. Scalmani, V. Barone, B. Mennucci, G. A. Petersson, H. Nakatsuji, M. Caricato, X. Li, H. P. Hratchian, A. F. Izmaylov, J. Bloino, G. Zheng, J. L. Sonnenberg, M. Hada, M. Ehara, K. Toyota, R. Fukuda, J. Hasegawa, M. Ishida, T. Nakajima, Y. Honda, O. Kitao, H. Nakai, T. Vreven, J. A. Montgomery Jr, J. E. Peralta, F. Ogliaro, M. Bearpark, J. J. Heyd, E. Brothers, K. N. Kudin, V. N. Staroverov, R. Kobayashi, J. Normand, K. Raghavachari, A. Rendell, J. C. Burant, S. S. Iyengar, J. Tomasi, M. Cossi, N. Rega, J. M. Millam, M. Klene, J. E. Knox, J. B. Cross, V. Bakken, C. Adamo, J. Jaramillo, R. Gomperts, R. E. Stratmann, O. Yazyev, A. J. Austin, R. Cammi, C. Pomelli, J. W. Ochterski, R. L. Martin, K. Morokuma, V. G. Zakrzewski, G. A. Voth, P. Salvador, J. J. Dannenberg, S. Dapprich, A. D. Daniels, Ö. Farkas, J. B. Foresman, J. V. Ortiz, J. Cioslowski and D. J. Fox, *Gaussian 09 (Revision A. 02)*, Gaussian Inc., Wallingford, CT, 2009.

31 K. Fukui, *Acc. Chem. Res.*, 1981, **14**, 363–368.

32 G. D. Purvis III and R. J. Bartlett, *J. Chem. Phys.*, 1982, **76**, 1910–1918.

33 D. G. Truhlar and B. C. Garrett, *Annu. Rev. Phys. Chem.*, 1984, **35**, 159–189.

34 M. Baradyn and A. Ratkiewicz, *J. Phys. Chem. A*, 2019, **123**, 750–763.

35 J. Zheng, J. L. Bao, R. Meana-Pañeda, S. Zhang, B. J. Lynch, J. C. Corchado, Y. Y. Chuang, P. L. Fast, W. P. Hu, Y. P. Liu, G. C. Lynch, K. A. Nguyen, C. F. Jackels, A. F. Ramos, B. A. Ellingson, V. S. Melissas, J. Villà, I. Rossi, E. L. Coitiño, J. Pu, T. V. Albu, A. Ratkiewicz, R. Steckler, B. C. Garrett, A. D. Isaacson and D. G. Truhlar, *Polyrate 17-C: Computer Program for the Calculation of Chemical Reaction Rates for Polyatomics*, University of Minnesota, Minneapolis, 2018.

36 M. L. Wei, X. F. Tan, Z. W. Long and B. Long, *RSC Adv.*, 2017, **7**, 56211–56219.

37 Y. Guo, Z. Y. Huang, G. Tian, W. Wu and X. L. Chang, *RSC Adv.*, 2023, **13**, 12469.

38 J. M. Anglada, J. González and M. Torrent-Sucarrat, *Phys. Chem. Chem. Phys.*, 2011, **13**, 13034–13045.

39 C. A. Taatjes, O. Welz, A. J. Eskola, J. D. Savee, A. M. Scheer, D. E. Shallcross, B. Rotavera, E. P. F. Lee, J. M. Dyke, D. K. W. Mok, D. L. Osborn and C. J. Percival, *Science*, 2013, **340**, 177–180.
40 B. N. Du and W. C. Zhang, *Molecules*, 2020, **35**, 3041.
41 L. Vereecken, H. Harder and A. Novelli, *Phys. Chem. Chem. Phys.*, 2012, **14**, 14682–14695.
42 M. Khan, M. Ashfold, G. Nickless, D. Martin, L. Watson, P. Hamer, R. Wayne, C. Canosa-Mas and D. Shallcross, *Atmos. Sci. Lett.*, 2008, **9**, 140–146.
43 R. F. Hansen, T. R. Lewis, L. Graham, L. K. Whalley, P. W. Seakins, D. E. Heard and M. A. Blitz, *Phys. Chem. Chem. Phys.*, 2017, **19**, 2332–2345.